Enabling the Internet of Bodies Through Capacitive Body Channel Access Schemes

Abdulkadir Celik [1] and Ahmed Eltawil [2]

[1]King Abdullah University of Science and Technology (KAUST)
[2]Affiliation not available

October 30, 2023

Abstract

The Internet of Bodies (IoB) is an imminent extension of the vast Internet of things (IoT) domain, where wearable, ingestible, injectable, and implantable smart objects form a network in, on, and around the human body. Even though on-body IoB communications are required to occur within very close proximity of the human body, on-body wireless radio frequency (RF) IoB devices unnecessarily extend the coverage range beyond the human body due to their radiative nature. This eventually reduces energy efficiency, causes co-existence and interference issues, and exposes sensitive personal data to security threats. Alternatively, capacitive body channel communications (BCC) exhibit much less signal leakage by confining signal transmission to the human body and experience substantially less propagation loss than RF systems as body tissues has better conductivity than surrounding air. Furthermore, the BCC band (10-100 MHz) decouples the transceiver size from the carrier wavelength, eliminating the need for complex and power-hungry radio front-ends. Therefore, capacitive BCC is a key enabler to reach the ultimate design goals of ultra-low-power, high throughput, and small form-factor IoB devices. Albeit these attractive features, the communication and networking aspects of the capacitive BCC are not thoroughly explored yet. This paper is the first to model orthogonal and non-orthogonal body channel access schemes with or without cooperation among the IoB nodes. In order to address the quality of service (QoS) demand scenarios of different IoB applications, we present and formulate max-min rate, max-sum rate, and QoS sufficient operational regimes, then provide solution methodologies for optimal power and phase time allocations. Extensive numerical results are analyzed to compare the performance of orthogonal and non-orthogonal schemes with and without cooperation for various design parameters under prescribed QoS regimes.

Enabling the Internet of Bodies Through Capacitive Body Channel Access Schemes

Abdulkadir Celik, *Senior Member, IEEE*, and Ahmed M. Eltawil, *Senior Member, IEEE*.

***Abstract*— The Internet of Bodies (IoB) is an imminent extension of the vast Internet of things (IoT) domain, where wearable, ingestible, injectable, and implantable smart objects form a network in, on, and around the human body. Even though on-body IoB communications are required to occur within very close proximity of the human body, on-body wireless radio frequency (RF) IoB devices unnecessarily extend the coverage range beyond the human body due to their radiative nature. This eventually reduces energy efficiency, causes co-existence and interference issues, and exposes sensitive personal data to security threats. Alternatively, capacitive body channel communications (BCC) exhibit much less signal leakage by confining signal transmission to the human body and experience substantially less propagation loss than RF systems as body tissues has better conductivity than surrounding air. Furthermore, the BCC band (10-100 MHz) decouples the transceiver size from the carrier wavelength, eliminating the need for complex and power-hungry radio front-ends. Therefore, capacitive BCC is a key enabler to reach the ultimate design goals of ultra-low-power, high throughput, and small form-factor IoB devices. Albeit these attractive features, the communication and networking aspects of the capacitive BCC are not thoroughly explored yet. This paper is the first to model orthogonal and non-orthogonal body channel access schemes with or without cooperation among the IoB nodes. In order to address the quality of service (QoS) demand scenarios of different IoB applications, we present and formulate max-min rate, max-sum rate, and QoS sufficient operational regimes, then provide solution methodologies for optimal power and phase time allocations. Extensive numerical results are analyzed to compare the performance of orthogonal and non-orthogonal schemes with and without cooperation for various design parameters under prescribed QoS regimes.**

***Index Terms*— Body area networks, intrabody communication, capacitive coupling, human body communication, galvanic coupling, non-orthogonal multiple access, cooperative communications, power control, relaying.**

I. Introduction

THE Internet of Bodies (IoB) is a forthcoming extension to the immense Internet of Things (IoT) domain, where uniquely identifiable smart objects (e.g., wearable, ingestible, injectable, and implantable) are interconnected to form a network in, on and around the human body [1]. Having its root in wireless body area networks (WBANs) [2], the IoB can transform our perception of various sectors, such as medicine, public health & safety, wellness, fitness, and cybersecurity, to name a few. The IEEE 802.15.6 standard defines physical and medium-access layer specifications to meet the distinct quality of service requirements in terms of throughput, latency, and power efficiency [3]. To this end, the IEEE 802.15.6 standard specifies three potential wireless technologies: narrowband (NB) and ultra-wideband (UWB) radio frequency (RF) communications, and body channel communications (BCC).

Authors are with the Computer, Electrical and Mathematical Sciences and Engineering Division, King Abdullah University of Science and Technology, Thuwal, KSA 23955-6900.

The NB and UWB systems perform significantly differently because of the electromagnetic signals' disparate propagation characteristics over channels in, on, and around the human body. This is mainly because of the lossy, frequency-dependent, and heterogeneous dielectric properties of human body tissues. Although NB and UWB systems are mature technologies with their own virtues in relation to different link types (e.g., in-body and on-body) and propagation modes (e.g., line of sight and non-line of sight), they are not the best option for on-body communications due to the following drawbacks:

- Nearby RF devices operating at the same band cause interference and co-existence issues. This is an especially challenging issue for the license-free industrial, scientific and medical (ISM) band, which is rapidly becoming saturated and interference limited by the ever increasing number of IoT devices.
- The radio front end is one of the most complex and power-hungry sub-systems of RF devices, which limits the node lifetime and requires a larger battery size. Thus, resulting form factors and frequent charging degrade the quality of the user experience and hinder wide-scale adoption of RF-based IoB devices.
- RF communications inadvertently permit an eavesdropper to intercept or even alter the original data. Hence, it is vital to protect the privacy and confidentiality of sensitive personal information against overhearing, eavesdropping, and bio-hackers' attacks. Nonetheless, both system complexity and monetary cost increase with additional security measures, which negatively impacts the miniature, low-cost, and ultra-low-power IoB design goals.

All these disadvantageous attributes of RF communications are commonly due to its highly radiative and omnidirectional propagation nature. Even though the on-body transmission should be limited up to a few centimeters around the human body, RF can extend several meters beyond, thus yielding unnecessary power consumption and exposure to security threats. Alternatively, body channel communication (BCC) is a promising wireless technology that confines the signal propagation to the human body by using human skin tissues

as a transmission medium. The transmitter electrodes couple electro-static fields to the body, which is captured by the receiver electrodes. Since biological tissues are more conductive than air, the BCC principally experiences a lower path loss (PL) and thus requires significantly less transmission power [4]. Compared to a 40-55 dB BCC path loss over a 1 m distance, a 2.4 GHz RF device experiences an up to 85 dB path loss as a result of the body shadowing effect [5]. The BCC is specifically designated to operate between 100 kHz and 100 MHz for two reasons [6]: 1) frequencies lower than 100 kHz are susceptible to electromagnetic interference and 2) at frequencies above 100 MHz, the human body acts as an antenna since the carrier wavelength approaches the length of human body parts. This specific band also determines two main BCC advantages. [7]:

- The BCC has negligible signal leakage as the transmission is confined to the human body. Noting that the BCC channel already operates out of RF bands, its low signal leakage level prevents interference and coexistence issues among IoB devices operating on nearby bodies. Since the BCC exploits the human body as a channel, it offers the physical layer security attributes of wired communications. This intuitively eliminates the need for complex and power-consuming signal processing components and security algorithms.
- Since the human body does not act as an antenna below 100 MHz, carrierless communication is possible as the transceiver size can be decoupled from the carrier wavelength, which eliminates the need for complex and power-hungry radio front-ends. Moreover, considering the substantially lower path loss, BCC can principally deliver throughput and energy-efficient communications with small form factor transceivers.

Galvanic coupling (GC) and capacitive coupling (CC) are the two most common signal transmission schemes adopted by BCC systems. In the former, both signal and ground electrodes of transceivers are in contact with the skin surface. Small currents passed between transmitter electrodes are detected by the receiver electrodes. In the latter, only signal electrodes are attached to the skin, while the floating ground electrodes form the return path through the environment [c.f. Fig. 1]. Since the signal (forward) path experiences low signal attenuation due to the conductivity of body tissues, the channel loss is mainly dominated by over-the-air capacitive return (backward) paths. Since GC–BCC's path loss characteristics limit its use to relatively low frequencies, it cannot support high-throughput and long-range communications. We therefore focus our attention on capacitive BCC, as it has been shown to exhibit better channel gains at higher frequencies and has already been adopted by the IEEE 802.15.6 Standard to deliver high data rates at very low transmission power levels [3].

A. Related Works and Main Contributions

The recent research efforts mainly focus on channel modeling and transceiver design aspects of the CC-BCC. The capacitive body channels models can be analytical, circuit-based, numerical, and empirical. Since the channel modeling

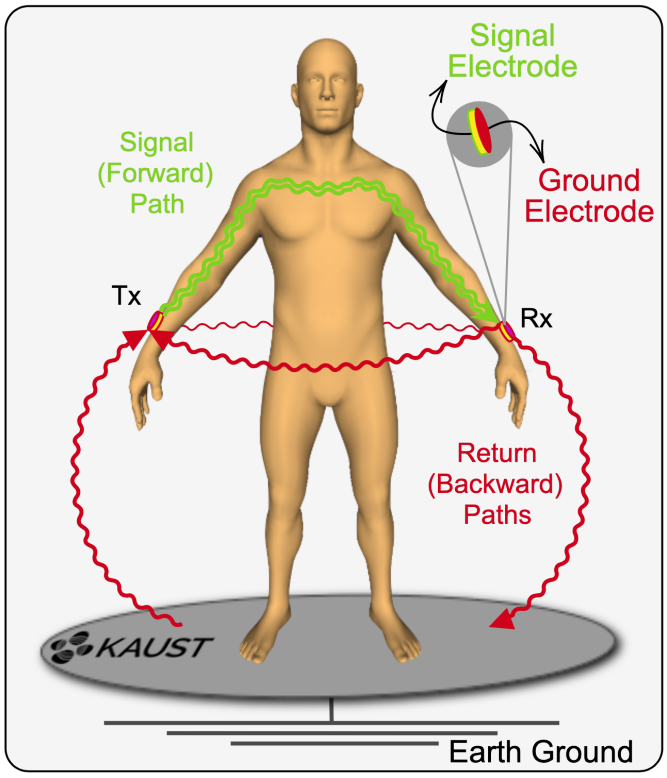

Fig. 1: Illustration of signal and return paths of capacitive body channel communications.

is out of this paper's scope, we refer interested readers to [1] for a systematic survey on propagation characterization and channel modeling of GC and CC body channels. The state-of-the-art transceiver designs have also shown that CC-BCC systems can reach energy efficiency levels ranging between 1nJ/b to 10pJ/b. In [8] Cho et. al. presented a 79 pJ/b 80 Mbps full-duplex transceiver along with a 42.5 μW 100 Kbps super-regenerative transceiver. In [9], Maity et al. developed a broadband interference tolerant transceiver that can achieve 6.3 pJ/b energy efficiency and 30 Mbps data rate by using time-domain interference rejection. In [10], Lee et al. design a 5580 μm^2 CMOS transceiver that can reach maximum data rates of 150 Mbps and 100 Mbps over 20 cm and 1 m CC-BCC channel lengths at costs of 16.6 pJ/b and 23.5 pJ/b, respectively. For a better data rate and energy efficiency comparison between the state-of-the-art transceiver designs, we refer interested readers to Fig. 1 and Fig. 17 of [8] and [9], respectively.

Although the aforementioned CC-BCC advantages are proven by these valuable contributions on channel characterization and ultra-low-power and high throughput transceiver designs, its communication and networking aspects are still not studied thoroughly. Accordingly, this paper is the first to conduct a full-scale investigation into the capacitive body channel access schemes for a generic IoB network, where a hub IoB node (e.g., smartwatch) aggregates data from several IoB nodes distributed across the body. To this aim, we model both orthogonal body channel access (OBA) and non-orthogonal body channel access (NOBA) schemes. While the

former dedicates equipartitioned bandwidths to each node, the latter multiplexes multiple nodes with different transmission powers on the total available bandwidths. In this way, the hub device can improve the spectral efficiency by executing successive interference decoding. The innate ability of non-orthogonal access schemes to avoid collisions can enable the use of simple and effective medium access control (MAC) protocols required by ultra-low-power and low complexity IoB nodes. Therefore, this paper provides analytical and numerical power control techniques to optimize the IoB network to meet quality of service (QoS) demands of different applications by utilizing the following operational regimes:

- Max-min rate regime aims at improving overall network performance by maximizing the throughput of the worst-performing node, which naturally forces other nodes' rates down and eventually yields a unique data rate for the entire IoB network. Therefore, this regime is beneficial for IoB applications where nodes disseminate data at the maximum achievable identical rates.
- Max-sum rate regime targets maximizing the network sum-rate while satisfying individual QoS requirements of each node. Therefore, the max-sum throughput scheme is especially beneficial for IoB applications where heterogeneous node types fulfill different tasks and need distinct QoS demands.
- QoS sufficient regime's sole purpose is to fulfill the exact QoS demand of each node to increase network life time. Therefore, this regime can be regarded as a mediocre solution between max-min and max-sum regimes if all nodes demand the same QoS levels.

These are further extended to cooperative OBA (C-OBA) and cooperative NOBA (C-NOBA) schemes. During the cooperation, the time-slot is divided into two phases and a source node closer to the hub decodes and forwards the messages received from far-away nodes during the first phase. In order to optimize the end-to-end performance, we also provide analytical and numerical phase time allocation optimization methods along with the optimal power controls. Numerical results show that NOBA can deliver better performance under certain circumstances. The power efficacy of NOBA improves as the QoS demand of nodes increases. The max-min rate gain of the NOBA scheme becomes significant if the worse channel gain node is located far away from the destination node, where the cooperation is shown to be beneficial to improve the max-min rate. On the other hand, the max-sum rate gain of NOBA constantly improves with increasing transmission power. However, its gain diminishes as the channel gain of the far-away nodes decreases. Unlike the max-min rate regime, cooperation is shown to deliver poorer performance than its regular counterparts as sharing the relay node's limited transmission power constitutes a bottleneck.

B. Paper Organization

The remainder of this paper is organized as follows: Section II presents the system models for orthogonal and non-orthogonal capacitive body channel access schemes with and without cooperation. Section III and Section IV present the power control and phase time allocation techniques for max-min rate and max-sum/QoS sufficient regimes, respectively. Section V presents numerical results and compares access schemes under different regimes. Lastly, Section VI concludes the paper with a few remarks.

II. Capacitive Body Channel Access

We consider the time-slotted operation of a generic IoB network, which consists of a destination IoB node located on the right wrist (e.g., smartwatch) and M source IoB nodes distributed across the body. The destination node n_d is responsible for coordination and management of the IoB network and acts as an access point (hub) to exchange necessary information with off-body entities through RF communications (e.g., Wi-Fi, BLE, etc.). The time-slot duration and total available bandwidth are denoted by T and B, respectively. The maximum transmission power of i^{th} source node, $n_i, \forall i$, is represented by $P_i \leqslant \bar{P}$, where $\bar{P}$ ensures that maximum power dissipation levels comply with health and safety regulations. Moreover, the channel gain between nodes n_i and n_j is denoted by h_i^j, which is obtained by finite element method (FEM) based simulations as explained in Section V-A.

In the remainder of this section, we present orthogonal and non-orthogonal body channel access methods with and without cooperation. Sets and their cardinality are denoted with calligraphic and regular uppercase letters (e.g., $|\mathcal{X}| = X$), respectively. Vectors and matrices are represented in lowercase and uppercase boldfaces (e.g., $\boldsymbol{x}$ and $\boldsymbol{X}$), respectively. Moreover, we use $\dot{x}$ and $\ddot{x}$ notations for orthogonal and non-orthogonal schemes, respectively, to distinguish between metrics and variables defined for both.

A. Regular Orthogonal Body Channel Access

In the regular OBA, source IoB nodes directly communicate with the destination on dedicated equipartitioned bandwidths of B/M over the entire time slot duration of T [c.f. Fig. 2.a]. The destination node n_d receives n_i's transmitted signal as

$$y_i^d = \sqrt{P_i h_i^d \dot{\omega}_i^d} x_i + z_i,\ i \in \mathcal{M} \tag{1}$$

where $\mathcal{M} = \left\{i : h_i^d > h_j^d, \forall j < i, (i,j) \in [1, M]\right\}$ represents the index set of source nodes sorted in descending order of the channel gains, $\dot{\omega}_i^d$ is the power allocation factor, x_i is the message of n_i*, $z_i \sim \mathcal{N}(0, N_0 B/M)$ is the additive white Gaussian noise, and N_0 is the thermal noise power spectral density. According to Shannon–Hartley theorem, the maximum achievable data rate over a noisy channel is given by

$$\dot{R}_i^d(\dot{\omega}_i^d) = \frac{B}{M} \log_2\left(1 + \dot{\gamma}_i^d(\dot{\omega}_i^d)\right), i \in \mathcal{M} \tag{2}$$

where $\dot{\gamma}_i^d(\dot{\omega}_i) = \frac{P_i h_i^d \dot{\omega}_i^d}{N_0 B/M}$ is the received signal-to-noise-ratio (SNR) at n_i receiver.

*Without loss of generality, we assume $E\{|x_i|^2\} = 1,\ \forall i$, throughput the paper.

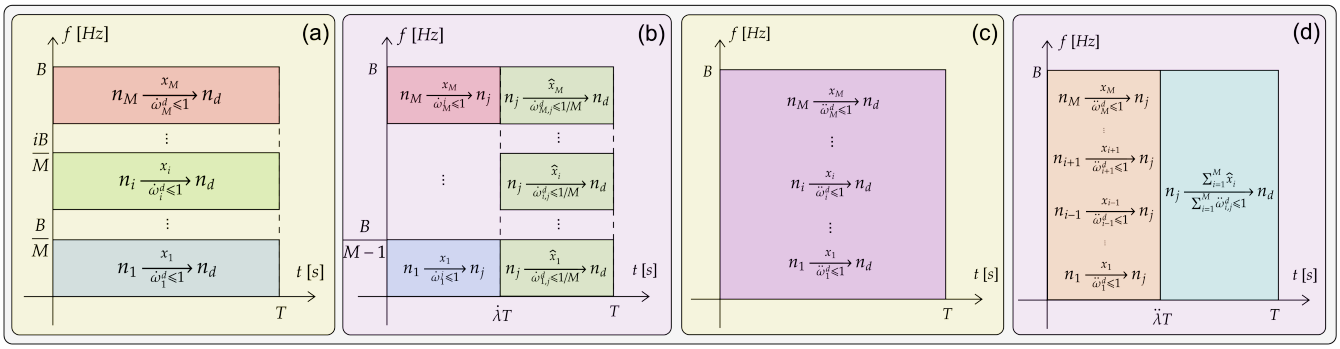

Fig. 2: Illustration of the capacitive body channel access schemes: a) regular orthogonal, b) cooperative orthogonal, c) regular non-orthogonal, and d) cooperative non-orthogonal.

B. Cooperative Orthogonal Body Channel Access

As shown in Fig. 2.b, the C-OBA divides the time slot into two phases. In the former, the relay node n_j stays idle and decodes messages sent by $M-1$ source nodes over $\dot{\lambda}T$ time duration. In the latter, source nodes switches to idle mode whereas the relay node forwards received messages along with its own to the destination node n_d over the remaining time slot duration, $(1-\dot{\lambda})T$. Notice in Fig. 2.b that the relay node equally divides available bandwidth and transmission power among all nodes, including itself, to keep the essence of orthogonality. Thus, the signal received by the relay node n_j is given by

$$y_i^j = \sqrt{P_i h_i^j \dot{\omega}_i^j} x_i + z_i,\ i \in \mathcal{M}_{-j} \tag{3}$$

where $z_i \sim \mathcal{N}(0, N_0 B/(M-1))$ and $\mathcal{M}_{-j} = \mathcal{M}\backslash\{j\}$ represents the set of source nodes excluding the relay node n_j. Similar to (1) and (2), the achievable data rates in the first phase are given by

$$\dot{R}_i^j\left(\dot{\omega}_i^j\right) = \frac{B}{M-1}\log_2\left(1+\dot{\gamma}_i^j\left(\dot{\omega}_i^j\right)\right),\ i \in \mathcal{M}_{-j} \tag{4}$$

where $\dot{\gamma}_i^j\left(\dot{\omega}_i^j\right) = \frac{P_i h_i^j \omega_i^j}{N_0 B/(M-1)}$ follows from (3). Notice in (3) and (4) that the entire bandwidth is shared only by nodes within $\mathcal{M}_{-j}$ as the relay node is silent during the first phase. In the second phase, the signals received by the destination node are given by

$$y_{i,j}^d = \sqrt{P_j h_j^d \dot{\omega}_{i,j}^d}\hat{x}_i + n_i,\ i \in \mathcal{M}, \tag{5}$$

where $\hat{x}_i$ is the decoded message of n_i, $\omega_{i,j}^d$ is the power allocated by n_j to relay n_i's messages, and $z_i \sim \mathcal{N}(0, N_0 B/M)$. Accordingly, relaying rates in the second phase are given by

$$\dot{R}_{i,j}^d\left(\dot{\omega}_{i,j}^d\right) = \frac{B}{M}\log_2\left(1+\dot{\gamma}_{i,j}^d\left(\dot{\omega}_{i,j}^d\right)\right), i \in \mathcal{M} \tag{6}$$

where $\dot{\gamma}_{i,j}^d\left(\dot{\omega}_{i,j}^d\right) = \frac{P_j h_j^d \dot{\omega}_{i,j}^d}{N_0 B/M}$ follows from (5). Based on (4) and (6), the end-to-end data rates are given by

$$\dot{R}_i^d\left(\lambda, \dot{\omega}_i^j, \dot{\omega}_{i,j}^d\right) = \min\left(\dot{\lambda}\dot{R}_i^j\left(\dot{\omega}_i^j\right), (1-\dot{\lambda})\dot{R}_{i,j}^d\left(\dot{\omega}_{i,j}^d\right)\right) \tag{7}$$

where $\dot{R}_j^j\left(\dot{\omega}_j^j\right) \triangleq \infty$ as n_j does not involve in transmission during the first phase.

C. Regular Non-Orthogonal Body Channel Access

In the regular NOBA, all nodes simultaneously transmit over the entire bandwidth B and time slot duration T [c.f. Fig. 2.c]. Therefore, the destination node receives a superposition of weighted transmit signals, which is given by

$$y_d = \sum_{i\in\mathcal{M}} \sqrt{P_i h_i^d \ddot{\omega}_i^d} x_i + z_i, \tag{8}$$

where $z_i \sim \mathcal{N}(0, N_0 B)$ and $\ddot{\omega}_i^d$ is determined to ensure that each message is delivered at distinct received power levels. In this way, the destination node can perform successive interference cancellation (SIC) to decode and subtract messages in the received power levels' descending order. In this way, a node enjoys the cancellation of interference from previously decoded messages while suffering from the interference caused by messages decoded afterward. The decoding order is governed by power allocation variables and plays an important role in reaping SIC's full benefits by allocating more (less) power to nodes experiencing high (less) interference. In this way, NOBA can improve the spectral efficiency while constituting a fairness among the nodes. It is shown in [11], [12] that uplink decoding order should follow the descending order of channel gains, i.e.,

$$\underbrace{\ddot{\omega}_M^d h_M^d < \ldots <}_{\text{uncancelable}} \ddot{\omega}_i^d h_i^d \underbrace{< \ldots < \ddot{\omega}_1^d h_1^d}_{\text{cancelable}} \tag{9}$$

$\mathcal{O}_l^i$: Lower Rank Decoding Order; $\mathcal{O}_h^i$: Higher Rank Decoding Order

where $\mathcal{O}_h^i$ and $\mathcal{O}_l^i$ are index set of nodes that belong to higher and lower rank decoding order of n_i, respectively. Accordingly, the received signal-to-interference-plus-noise (SINR) and achievable throughput of n_i are respectively given by

$$\ddot{\gamma}_i^d\left(\ddot{\boldsymbol{\omega}}\right) = \frac{P_i h_i^d \ddot{\omega}_i^d}{\sum_{\substack{k>i\\ k\in\mathcal{M}}} P_k h_k^d \ddot{\omega}_k^d + N_0 B}, \text{ and} \tag{10}$$

$$\ddot{R}_i^d\left(\ddot{\boldsymbol{\omega}}\right) = B\log_2\left(1+\ddot{\gamma}_i^d\left(\ddot{\boldsymbol{\omega}}\right)\right), i \in \mathcal{M}, \tag{11}$$

where $\ddot{\boldsymbol{\omega}} = [\ddot{\omega}_1^d, ..., \ddot{\omega}_i^d, ..., \ddot{\omega}_M^d]$ is the vector of power allocation factors.

D. Cooperative Non-Orthogonal Body Channel Access

As shown in Fig. 2.b, the C-NOBA also divides the time slot into two phases. In the former, the relay node n_j successively decodes superposed messages sent by other source nodes over $\ddot{\lambda}T$ time duration. In the latter, the relay node n_j broadcasts received messages along with its own to the destination node n_d in the remaining time slot duration, $(1-\ddot{\lambda})T$. Notice in Fig. 2.d that the first phase is identical to the regular case in Fig. 2.c, except that n_j is silent to listen and successively decode messages sent by other nodes. Following similar steps to obtain (11), the received SINR and data rate after SIC operations are respectively given by

$$\ddot{\gamma}_i^j\left(\ddot{\boldsymbol{\omega}}_{\mathbf{1}}\right)=\frac{P_i h_i^j \ddot{\omega}_i^j}{\sum_{\substack{k>i\\ k\in\mathcal{M}_{-j}}} P_k h_k^j \ddot{\omega}_k^j + N_0 B}, \text{ and} \tag{12}$$

$$\ddot{R}_i^j\left(\ddot{\boldsymbol{\omega}}_{\mathbf{1}}\right)=B\log_2\left(1+\ddot{\gamma}_i^j\left(\ddot{\boldsymbol{\omega}}_{\mathbf{1}}\right)\right), i\in\mathcal{M}_{-j}, \tag{13}$$

where $\ddot{\boldsymbol{\omega}}_{\mathbf{1}}=[\ddot{\omega}_1^d,...,\ddot{\omega}_{j-1}^d,\ddot{\omega}_{j+1}^d,...,\ddot{\omega}_M^d]$ is the vector of power allocation factors of the first phase.. In the second phase, source nodes stays idle and the relay node broadcasts successively decoded and weighted messages, which is received by the destination as

$$y_d=\sum_{i\in\mathcal{M}}\sqrt{P_j h_j^d \ddot{\omega}_{i,j}^d}\hat{x}_i+z_i, \tag{14}$$

where $z_i\sim\mathcal{N}(0,N_0B)$. The destination node n_d also performs SIC procedure, which respectively yields the following SINRs and data rates

$$\ddot{\gamma}_{i,j}^d\left(\ddot{\boldsymbol{\omega}}_{\mathbf{2}}\right)=\frac{P_j h_j^d \ddot{\omega}_{i,j}^d}{\sum_{\substack{k>i\\ k\in\mathcal{M}}} P_j h_j^d \ddot{\omega}_{k,j}^d + N_0 B}, \text{ and} \tag{15}$$

$$\ddot{R}_{i,j}^d\left(\ddot{\boldsymbol{\omega}}_{\mathbf{2}}\right)=B\log_2\left(1+\ddot{\gamma}_{i,j}^d\left(\ddot{\boldsymbol{\omega}}_{\mathbf{2}}\right)\right), i\in\mathcal{M}, \tag{16}$$

where $\ddot{\boldsymbol{\omega}}_{\mathbf{2}}=[\ddot{\omega}_{1,j}^d,...,\ddot{\omega}_{i,j}^d,...,\ddot{\omega}_{M,j}^d]$ is the vector of power allocation factors in the second phase. Lastly, the end-to-end data rates for n_i is given by

$$\ddot{R}_i^d(\ddot{\lambda},\ddot{\boldsymbol{\omega}}_{\mathbf{1}},\ddot{\boldsymbol{\omega}}_{\mathbf{2}})=\min\left(\ddot{\lambda}\ddot{R}_i^j\left(\ddot{\boldsymbol{\omega}}_{\mathbf{1}}\right),(1-\ddot{\lambda})\ddot{R}_{i,j}^d\left(\ddot{\boldsymbol{\omega}}_{\mathbf{2}}\right)\right), \forall i\in\mathcal{M} \tag{17}$$

where $\ddot{R}_j^j\left(\ddot{\boldsymbol{\omega}}_{\mathbf{1}}\right)\triangleq\infty$ as n_j is not involved in transmission during the first phase.

III. Max-Min Rate Regime

In the max-min throughput scheme, we are interested in improving overall network performance by maximizing throughput of the worst performing node. This is also known as max-min fairness as pushing the worst performing node's rate up naturally forces other nodes' rates down, which eventually results in equal data rates for the entire IoB network. Therefore, max-min fair regime is especially useful for IoB applications where nodes distributed across the body disseminate data at the maximum identical data rates. Although the max-min fairness can be achieved by controlling transmission power in regular access schemes, the cooperative access schemes require joint optimization of power and phase time allocations.

A. Max-Min Fair Orthogonal Body Channel Access

The max-min fair power allocation of the regular orthogonal body channel access can be formulated as

$$\mathbf{P_{mm}^{ro}}:\ \max_{\mathbf{0}\preceq\dot{\boldsymbol{\omega}}\preceq\mathbf{1}}\min_{i\in\mathcal{M}}\left(\dot{R}_i^d\left(\omega_i^d\right)\right), \tag{18}$$

where $\mathbf{0}$ is a vector of zeros, $\mathbf{1}$ is a vector of ones, and $\preceq$ is the pairwise inequality operator. The optimal solution of $\mathbf{P_{mm}^{ro}}$ is reached at $\dot{R}_M^d(1)$ by setting the power allocation factor of the lowest channel gain node, n_M, to unity, $\dot{\omega}_M^{d,\star}=1$. The remaining nodes must also transmit at a rate no less than $\dot{R}_M^d(1)$ by adjusting their power allocation factors to

$$\dot{\omega}_i^{d,\star}\geqslant\left(2^{\frac{M\dot{R}_M^d(1)}{B}}-1\right)\frac{N_0B}{MP_ih_i^d}, \forall i\in\mathcal{M}_{-j}, \tag{19}$$

which follows from solving $\dot{R}_M^d(\dot{\omega}_i^d)\geqslant\dot{R}_M^d(1)$ for $\dot{\omega}_i^d$, $\forall i\in\mathcal{M}_{-j}$. Similarly, the max-min fair C-OBA can be formulated as

$$\mathbf{P_{mm}^{co}}:\ \max_{\substack{\mathbf{0}\preceq\dot{\lambda},\dot{\boldsymbol{\omega}}_{\mathbf{1}}\preceq\mathbf{1}\\ \mathbf{0}\preceq\dot{\boldsymbol{\omega}}_{\mathbf{2}}\preceq\mathbf{1}/M}}\min_{i\in\mathcal{M}}\left(\dot{R}_i^d(\lambda,\dot{\boldsymbol{\omega}}_{\mathbf{1}},\dot{\boldsymbol{\omega}}_{\mathbf{2}})\right), \tag{20}$$

which can be decoupled as variables do not complicate each other. That is, an optimal λ can be obtained based on the power weights that maximizes each phase's SNR, i.e., rate. Denoting the lowest channel gain node within $\mathcal{M}_{-j}$ by n_k, the optimal max-min rate of the first phase is given by $\dot{R}_k^j(1)$, which requires remaining nodes to adjust their power allocation factors as follows

$$\dot{\omega}_i^{d,\star}\geqslant\left(2^{\frac{(M-1)\dot{R}_k^j(1)}{B}}-1\right)\frac{N_0B}{(M-1)P_ih_i^j}, i\in\mathcal{M}_{-\{j,k\}}. \tag{21}$$

Likewise, the optimal max-min rate of the second phase is given by $\dot{R}_{M,j}^d\left(\frac{1}{M}\right)$, which also requires n_j to adjust its power allocation factors as follows

$$\dot{\omega}_{i,j}^{d,\star}\geqslant\left(2^{\frac{M\dot{R}_{M,j}^d\left(\frac{1}{M}\right)}{B}}-1\right)\frac{N_0B}{MP_jh_j^d}, i\in\mathcal{M}. \tag{22}$$

Since the end-to-end performance is determined by the minimum of two phases, the optimal solution of $\mathbf{P_{mm}^{co}}$ is attained by adjusting $\dot{\lambda}$ to equalize the individual max-min rate of the first and second phases, i.e., $\dot{\lambda}^\star\dot{R}_k^j(1)=(1-\dot{\lambda}^\star)\dot{R}_{M,j}^d\left(\frac{1}{M}\right)$, as follows

$$\dot{\lambda}^\star=\frac{\dot{R}_{M,j}^d\left(\frac{1}{M}\right)}{\dot{R}_k^j(1)+\dot{R}_{M,j}^d\left(\frac{1}{M}\right)}. \tag{23}$$

It is worth noting that optimal power allocations $\dot{\omega}_i^{d^\star}$ in (19)-(21) and $\dot{\omega}_{i,j}^{d^\star}$ in (22) should be satisfied at equality as there is no max-min rate enhancement by forcing nodes, other than the worst performing node, to transmit at higher rates at the expense of more power consumption.

B. Max-Min Fair Non-Orthogonal Body Channel Access

In the previous section, orthogonality grants an interference-free communication as nodes operate at dedicated bandwidths with their individual power sources. This naturally allowed us to derive optimal max-min rates and corresponding power allocation factors after some algebraic manipulations. However,

this is not the case for non-orthogonal body channel access due to the uncanceled interference terms in the denominator of the SINR expressions. By introducing an auxiliary variable ψ, the max-min fair regular NOBA problem can be formulated as

$$\begin{aligned} \mathbf{P^{rn}_{mm}}: & \max_{\ddot{\boldsymbol{\omega}},\psi} \quad \psi \\ \mathrm{C}_1: \quad & \text{s.t.} \quad \ddot{R}_i^d(\ddot{\omega}_i^d) \geqslant \psi, \ \forall i \\ \mathrm{C}_2: \quad & \mathbf{0} \preceq \ddot{\boldsymbol{\omega}} \preceq \mathbf{1}, \psi \geqslant 0, \end{aligned} \tag{24}$$

which obtains the optimal max-min rate by increasing ψ up while enforcing all nodes to transmit at a rate no less than ψ. Since uncancelable interference terms in (12) cause the elements of $\ddot{\boldsymbol{\omega}}$ to complicate each other, $\mathbf{P^{rn}_{mm}}$ does not have trivial solution as in the orthogonal case. Fortunately, it can be converted into a convex problem by putting its first constraint into the standard form of a geometric programming problem. In the standard form, equality constraints needs to be monomials, i.e., $f(x_1, x_2, \ldots, x_n) = x_1^{a_1} x_2^{a_2} \cdots x_n^{a_n}$, where $c > 0$ and $a_i \in \mathbb{R}$. On the other hand, objective function and inequality constraints are required to be sum of monomials (posynomials), i.e., $f(x_1, x_2, \ldots, x_n) = \sum_{k=1}^{K} c_k x_1^{a_{1k}} \cdots x_n^{a_{nk}}$, where $c_k > 0$ and $a_{ik} \in \mathbb{R}$. Accordingly, C_1 of (24) can be rewritten in the posynomial form as follows

$$\mathrm{C}_1: \psi \frac{\sum_{k \in \mathcal{M}_{-j}^{k>i}} P_k h_k^d \ddot{\omega}_k^d + N_0 B}{P_i h_i^d \ddot{\omega}_i^d} \leqslant 1. \tag{25}$$

On the other hand, the max-min fair C-NOBA problem is given by

$$\mathbf{P^{cn}_{mm}}: \max_{\mathbf{0} \preceq \ddot{\lambda}, \ddot{\boldsymbol{\omega}}_1, \ddot{\boldsymbol{\omega}}_2 \preceq \mathbf{1}} \min_{i \in \mathcal{M}} \left(\ddot{R}_i^d(\lambda, \ddot{\boldsymbol{\omega}}_1, \ddot{\boldsymbol{\omega}}_2) \right) \ \text{s.t.} \ \mathbf{1}^T \ddot{\boldsymbol{\omega}}_2 \leqslant 1, \tag{26}$$

which can also be decoupled into first and second phase optimization since $\ddot{\lambda}$, $\ddot{\boldsymbol{\omega}}_1$, and $\ddot{\boldsymbol{\omega}}_2$ do not complicate each other as in (20). Noting that the first phase power control problem $\mathbf{P^{cn}_{mm}}(\mathbf{1})$ is very similar to (24), the second phase power control can be formulated as

$$\begin{aligned} \mathbf{P^{cn}_{mm}}(\mathbf{2}): & \max_{\ddot{\boldsymbol{\omega}}_2, \psi_2} \quad \psi_2 \\ \mathrm{C}_1: \quad & \text{s.t.} \quad \ddot{R}_{i,j}^d(\ddot{\boldsymbol{\omega}}_2) \geqslant \psi_2, \ \forall i \\ \mathrm{C}_2: \quad & \sum_{i \in \mathcal{M}} \ddot{\omega}_{i,j}^d \leqslant 1, \\ \mathrm{C}_3: \quad & \mathbf{0} \preceq \ddot{\boldsymbol{\omega}}_2 \preceq \mathbf{1}, 0 \leqslant psi_2, \end{aligned} \tag{27}$$

where C_2 requires total allocated power by the relay node is less than unity and is already in the posynomial form. Once the optimal power allocations are obtained from $\mathbf{P^{cn}_{mm}}(\mathbf{1})$ and $\mathbf{P^{cn}_{mm}}(\mathbf{2})$, the individual max-min rate of the first and second phases are given by $\min_{i \in \mathcal{M}_{-j}} \left(\ddot{R}_i^j \left(\ddot{\boldsymbol{\omega}}_1^\star \right) \right)$ and $\min_{i \in \mathcal{M}} \left(\ddot{R}_{i,j}^d \left(\ddot{\boldsymbol{\omega}}_2^\star \right) \right)$, respectively. Accordingly, the optimal phase time allocation can be formulated as follows

$$\ddot{\lambda}^\star = \frac{\min_{i \in \mathcal{M}} \left(\ddot{R}_{i,j}^d \left(\ddot{\boldsymbol{\omega}}_2^\star \right) \right)}{\min_{i \in \mathcal{M}_{-j}} \left(\ddot{R}_i^j \left(\ddot{\boldsymbol{\omega}}_1^\star \right) \right) + \min_{i \in \mathcal{M}} \left(\ddot{R}_{i,j}^d \left(\ddot{\boldsymbol{\omega}}_2^\star \right) \right)}, \tag{28}$$

which is in favor of the phase with a lower individual max-min rate to maximize the end-to-end max-min rate and follows from

$$\ddot{\lambda}^\star \min_{i \in \mathcal{M}_{-j}} \left(\ddot{R}_i^j \left(\ddot{\boldsymbol{\omega}}_1^\star \right) \right) = (1 - \ddot{\lambda}^\star) \min_{i \in \mathcal{M}} \left(\ddot{R}_{i,j}^d \left(\ddot{\boldsymbol{\omega}}_2^\star \right) \right).$$

We should also note that $\mathbf{P^{rn}_{mm}}$, $\mathbf{P^{cn}_{mm}}(\mathbf{1})$, and $\mathbf{P^{cn}_{mm}}(\mathbf{1})$ can also be solved analytically by ignoring interference tolerance constraints in [13].

IV. Max-Sum Rate & QoS Sufficient Regimes

In the max-sum throughput regime, we are interested in improving network sum-rate while satisfying individual QoS requirements of each node. Therefore, max-sum throughput regime is especially useful for IoB applications where heterogeneous node types fulfill different functions and need specific QoS demands. Although the max-sum rate can be achieved by controlling transmission powers in regular access schemes, the cooperative access schemes require optimization of both power and phase time allocations. The max-sum rate regime can be reduced to a 'QoS sufficient' regime where nodes are only interested in satisfying QoS requirements in order to increase network life time. The QoS sufficient regime can also be regarded as a special case of the max-min fair regime if all nodes demand the same QoS levels. Throughout this section, we will not provide problem formulations for the QoS sufficient regimes since it follows the max-sum regime with a constant objective function instead of sum rates and QoS constraints to be satisfied at equality.

A. Orthogonal Body Channel Access

1) Max-Sum Rate Regime: Power allocation problem of the max-sum rate regime can be formulated as

$$\mathbf{P^{ro}_{ms}}: \max_{\mathbf{0} \preceq \dot{\boldsymbol{\omega}}_1 \preceq \mathbf{1}} \sum_{i \in \mathcal{M}} \dot{R}_i^d \left(\dot{\omega}_i^d \right) \ \text{s.t.} \ \dot{R}_i^d \left(\dot{\omega}_i^d \right) \geqslant \bar{R}_i^d \tag{29}$$

where $\bar{R}_i^d$ is the QoS demand of n_i, $\mathbf{0}$ is a vector of zeros, $\mathbf{1}$ is a vector of ones, and $\preceq$ is the pairwise inequality operator. The optimal solution of $\mathbf{P^{ro}_{ms}}$ is reached at $\sum_{i \in \mathcal{M}} \dot{R}_i^d(1)$ by forcing all nodes to transmit at maximum available power, i.e., $\dot{\omega}_i^{d,\star} = 1$, $i \in \mathcal{M}^\dagger$. Similar to the regular case, the max-sum rate regime C-OBA also requires nodes to transmit at maximum available power in both phases, i.e., $\dot{\omega}_i^{j,\star} = 1$, $i \in \mathcal{M}_{-j}$ and $\dot{\omega}_{i,j}^{d,\star} = 1/M$, $i \in \mathcal{M}$. Accordingly, the phase time allocation variable needs to be optimized to maximize overall sum-rate as follows

$$\dot{\boldsymbol{\lambda}}^{\mathbf{co}}_{\mathbf{ms}}: \max_{\lambda_l \leqslant \dot{\lambda} \leqslant \lambda_u} \sum_{i \in \mathcal{M}} \min \left(\dot{\lambda} \dot{R}_i^j \left(\dot{\omega}_i^{j,\star} \right), (1 - \dot{\lambda}) \dot{R}_{i,j}^d \left(\dot{\omega}_{i,j}^{d,\star} \right) \right) \tag{30}$$

where $\dot{\lambda}_l = \max_{i \in \mathcal{M}_{-j}} \left\{ \frac{\bar{R}_i}{\dot{R}_i^j \left(\dot{\omega}_i^{j,\star} \right)} \right\}$ and $\lambda_u = \min_{i \in \mathcal{M}} \left\{ \frac{\dot{R}_{i,j}^d \left(\dot{\omega}_{i,j}^{d,\star} \right) - \bar{R}_i}{\dot{R}_{i,j}^d \left(\dot{\omega}_{i,j}^{d,\star} \right)} \right\}$ follow from QoS constraints $\dot{\lambda} \dot{R}_i^d(\dot{\omega}_i^{j,\star}) \geqslant \bar{R}_i$ and $(1 - \dot{\lambda}) \dot{R}_{i,j}^d(\dot{\omega}_{i,j}^{d,\star}) \geqslant \bar{R}_i$, respectively. $\mathbf{P}_{\dot{\boldsymbol{\lambda}}}$ can be solved expeditiously by simple line search algorithms.

[†]In order to have a feasible network operation, a node should not demand a QoS more than its individual performance, i.e., $\bar{R}_i^d \leqslant \dot{R}_i^d(1)$, $\forall i \in \mathcal{M}$.

2) QoS Sufficient Regime: Instead of transmitting at maximum power levels, the regular QoS sufficient regime satisfies QoS constraints at equality by adjusting power allocation factors as follows

$$\dot{\omega}_i^{d,\star} = \left(2^{\frac{\bar{R}M}{B}} - 1\right) \frac{N_0 B}{M P_i h_i^d}, \forall i \in \mathcal{M}, \tag{31}$$

which is derived by solving $\dot{R}_i^d\left(\dot{\omega}_i^d\right) = \bar{R}$ for $\dot{\omega}_i^d$, $i \in \mathcal{M}$. On the other hand, the cooperative and orthogonal QoS sufficient regime requires each node to satisfy the QoS demand at both phases, which yields the following power and phase allocation factors

$$\dot{\omega}_i^{j,\star} = \left(2^{\frac{\bar{R}(M-1)}{\dot{\lambda}B}} - 1\right) \frac{N_0 B}{(M-1) P_i h_i^j}, \ \forall i \in \mathcal{M}_{-j}, \tag{32}$$

$$\dot{\omega}_{i,j}^{d,\star} = \left(2^{\frac{\bar{R}M}{(1-\dot{\lambda})B}} - 1\right) \frac{N_0 B}{M P_j h_j^d}, \ \forall i \in \mathcal{M}, \text{ and} \tag{33}$$

$$\dot{\lambda}^\star = \frac{1}{2}, \tag{34}$$

which are derived from $\dot{\lambda}\dot{R}_i^j\left(\dot{\omega}_i^{j,\star}\right) = \bar{R}$, $\forall i \in \mathcal{M}_{-j}$, $(1-\dot{\lambda})\dot{R}_{i,j}^d\left(\dot{\omega}_{i,j}^{d,\star}\right) = \bar{R}$, $\forall i \in \mathcal{M}$, and $\dot{\lambda}\bar{R} = (1-\dot{\lambda})\bar{R}$, respectively.

B. Non-Orthogonal Body Channel Access

1) Max-Sum Rate Regime: The max-sum regime of regular NOBA problem can be formulated as

$$\begin{aligned} \mathbf{P_{ms}^{rn}}: \max_{\ddot{\boldsymbol{\omega}}} \quad & \sum_{i\in\mathcal{M}} \ddot{R}_i^d(\ddot{\boldsymbol{\omega}}) \\ \mathrm{C}_1: \quad \text{s.t.} \quad & \ddot{R}_i^d(\ddot{\omega}_i^d) \geqslant \bar{R}_i^d, \ \forall i \\ \mathrm{C}_2: \quad & \mathbf{0} \preceq \ddot{\boldsymbol{\omega}} \preceq \mathbf{1}, \end{aligned} \tag{35}$$

which can be put into geometric programming problem by first transforming the max-sum rate objective into a product of posynomials as follows

$$\begin{aligned} &\max_{\ddot{\boldsymbol{\omega}}} \sum_{i\in\mathcal{M}} B\log_2\left(1+\ddot{\gamma}_i^d(\ddot{\boldsymbol{\omega}})\right) \overset{(a)}{\approx} \max_{\ddot{\boldsymbol{\omega}}} \sum_{i\in\mathcal{M}} \log_2\left(\ddot{\gamma}_i^d(\ddot{\boldsymbol{\omega}})\right) \\ &\overset{(b)}{=} \max_{\ddot{\boldsymbol{\omega}}} \log_2\left(\prod_{i\in\mathcal{M}} \ddot{\gamma}_i^d(\ddot{\boldsymbol{\omega}})\right) \overset{(c)}{=} \max_{\ddot{\boldsymbol{\omega}}} \prod_{i\in\mathcal{M}} \ddot{\gamma}_i^d(\ddot{\boldsymbol{\omega}}) \\ &\overset{(d)}{=} \min_{\ddot{\boldsymbol{\omega}}} \prod_{i\in\mathcal{M}} \frac{1}{\ddot{\gamma}_i^d(\ddot{\boldsymbol{\omega}})} \end{aligned} \tag{36}$$

where the approximation (a) is based on high SINR assumption. Sum of logarithms is the same with logarithm of products in (b) and the monotonicity of the logarithm makes the maximization of $\log(f(\cdot))$ equivalent to the maximization of $f(\cdot)$ as in (c). Lastly, (d) provides a posynomial by changing the objective from a maximum of SINR product to minimum of inverse SINR product. Accordingly, $\mathbf{P_{ms}^{rn}}$ in (35) can be rewritten as a geometric programming problem as follows

$$\begin{aligned} \mathbf{P_{ms}^{rn}}: \min_{\ddot{\boldsymbol{\omega}}} \quad & \prod_{i\in\mathcal{M}} \frac{1}{\ddot{\gamma}_i^d(\ddot{\boldsymbol{\omega}})} \\ \mathrm{C}_1: \quad \text{s.t.} \quad & \left(2^{\bar{R}_i^d/B} - 1\right) \frac{\sum_{k\in\mathcal{M}_{-j}^{k>i}} P_k h_k^d \ddot{\omega}_k^d + N_0 B}{P_i h_i^d \ddot{\omega}_i^d} \leqslant 1, \ \forall i \\ \mathrm{C}_2: \quad & \mathbf{0} \preceq \ddot{\boldsymbol{\omega}} \preceq \mathbf{1}, \end{aligned} \tag{37}$$

where C_1 is also put into the posynomial form as in (25).

On the other hand, the max-sum regime C-NOBA problem is given by

$$\mathbf{P_{ms}^{cn}}: \max_{\mathbf{0}\preceq\ddot{\lambda},\ddot{\boldsymbol{\omega}}_1,\ddot{\boldsymbol{\omega}}_2\preceq\mathbf{1}} \sum_{i\in\mathcal{M}} \left(\ddot{R}_i^d(\lambda, \ddot{\boldsymbol{\omega}}_1, \ddot{\boldsymbol{\omega}}_2)\right) \text{ s.t. } \mathbf{1}^T\ddot{\boldsymbol{\omega}}_2 \leqslant 1, \tag{38}$$

which can also be decoupled into the first and the second phase optimizations since $\ddot{\lambda}$, $\ddot{\boldsymbol{\omega}}_1$, and $\ddot{\boldsymbol{\omega}}_2$ do not complicate each other similar to (26). Noting that the first phase power control problem $\mathbf{P_{mm}^{cn}}(\mathbf{1})$ is very similar to (37), the second phase power control can be formulated as

$$\begin{aligned} \mathbf{P_{ms}^{cn}}(\mathbf{2}): \min_{\ddot{\boldsymbol{\omega}}_2} \quad & \prod_{i\in\mathcal{M}} \frac{1}{\ddot{\gamma}_{i,j}^d(\ddot{\boldsymbol{\omega}}_2)} \\ \mathrm{C}_1: \quad \text{s.t.} \quad & \left(2^{\bar{R}_i^d/B} - 1\right) \frac{\sum_{k\in\mathcal{M}_{-j}^{k>i}} P_j h_j^d \ddot{\omega}_{i,j}^d + N_0 B}{P_j h_j^d \ddot{\omega}_{i,j}^d} \leqslant 1, \ \forall i \\ \mathrm{C}_2: \quad & \sum_{i\in\mathcal{M}} \ddot{\omega}_{i,j}^d \leqslant 1, \\ \mathrm{C}_3: \quad & \mathbf{0} \preceq \ddot{\boldsymbol{\omega}}_2 \preceq \mathbf{1}, \end{aligned} \tag{39}$$

where C_2 requires total allocated power by the relay node is less than unity and is already in the posynomial form. We should note that $\mathbf{P_{ms}^{rn}}$ and $\mathbf{P_{ms}^{cn}}$ can also be solved by analytical methods as shown in [12], [14].

Once the optimal power allocations are obtained from $\mathbf{P_{ms}^{cn}}(\mathbf{1})$ and $\mathbf{P_{ms}^{cn}}(\mathbf{2})$, the optimal phase time allocation can be formulated similar to (30) as follows

$$\ddot{\boldsymbol{\lambda}}_{\mathbf{ms}}^{\mathbf{co}}: \max_{\lambda_l\leqslant\ddot{\lambda}\leqslant\lambda_u} \sum_{i\in\mathcal{M}} \min\left(\ddot{\lambda}\ddot{R}_i^j\left(\ddot{\omega}_i^{j,\star}\right), (1-\ddot{\lambda})\ddot{R}_{i,j}^d\left(\ddot{\omega}_{i,j}^{d,\star}\right)\right) \tag{40}$$

where $\ddot{\lambda}_l = \max_{i\in\mathcal{M}_{-j}}\left\{\frac{\bar{R}_i}{\ddot{R}_i^j(\ddot{\omega}_i^{j,\star})}\right\}$ and $\lambda_u = \min_{i\in\mathcal{M}}\left\{\frac{\ddot{R}_{i,j}^d(\ddot{\omega}_{i,j}^{d,\star})-\bar{R}_i}{\ddot{R}_{i,j}^d(\ddot{\omega}_{i,j}^{d,\star})}\right\}$ follow from QoS constraints $\ddot{\lambda}\ddot{R}_i^d(\ddot{\omega}_i^{j,\star}) \geqslant \bar{R}_i$ and $(1-\ddot{\lambda})\ddot{R}_{i,j}^d(\ddot{\omega}_{i,j}^{d,\star}) \geqslant \bar{R}_i$, respectively. $\mathbf{P}_{\ddot{\boldsymbol{\lambda}}}$ can also be solved expeditiously by simple line search algorithms.

2) QoS Sufficient Regime: For the regular QoS sufficient regime, the optimal power allocation factors can be obtained recursively based on the seminal work of Yates [15] as follows

$$\omega_1^{d,\star} = \frac{N_0 B\left(2^{\frac{\bar{R}}{B}} - 1\right) 2^{\left(\frac{\bar{R}}{B}\right)^{M-1}}}{P_1 h_1^d}, \tag{41}$$

$$\omega_i^{d,\star} = \frac{\omega_1^{d,\star} h_1^d}{h_i^d 2^{\left(\frac{\bar{R}}{B}\right)^{i-1}}}, 2 \leqslant i \leqslant M. \tag{42}$$

where recursion is due to the decoding order explained in Section II-C. In a similar manner, the first phase optimal power allocation factors of the cooperative scheme is given by

$$\omega_1^{j,\star} = \frac{N_0 B\left(2^{\frac{\bar{R}}{\dot{\lambda}B}} - 1\right) 2^{\left(\frac{\bar{R}_1}{\dot{\lambda}B}\right)^{M-2}}}{P_1 h_1^j}, \tag{43}$$

$$\omega_i^{j,\star} = \frac{\omega_1^{d,\star} h_1^j}{h_i^j 2^{\left(\frac{\bar{R}_i}{\dot{\lambda}B}\right)^{i-1}}}, 2 \leqslant i \leqslant M-1. \tag{44}$$

Likewise, the second phase optimal power allocation factors of the cooperative scheme is given by

$$\omega_{i,j}^{d,\star} = \frac{N_0 B \left(2^{\frac{\bar{R}_1}{(1-\ddot{\lambda})B}} - 1\right) 2^{\left(\frac{\bar{R}}{(1-\ddot{\lambda})B}\right)^{M-1}}}{P_1 h_j^d}, \tag{45}$$

$$\omega_{i,j}^{d,\star} = \frac{\omega_{i,j}^{d,\star}}{2^{\left(\frac{\bar{R}}{(1-\ddot{\lambda})B}\right)^{i-1}}}, 2 \leqslant i \leqslant M. \tag{46}$$

Since all users satisfy QoS constraints at equality, the optimal phase time allocation must be $\ddot{\lambda} = \frac{1}{2}$ as in the orthogonal QoS sufficient regime.

V. Numerical Results

In this section, we present numerical results to compare different body channel access schemes with and without cooperation under various operational regimes. Unless it is stated explicitly otherwise, we exploit the following parameters: maximum transmission power $P_i = -60$ dBm, $\forall i$, total network bandwidth $B = 1$ MHz, time slot duration $T = 1$ s, the noise power spectral density $N_0 = -174$ dBm/Hz, and operational frequency $f = 65$ MHz. Unless stated explicitly otherwise, all results are generated and plotted by Matlab in the rest of this section. We also use CVX's Matlab toolbox for the geometric programming [16].

A. Parametric Channel Model of the Capacitive BCC

Since capacitive BCC interacts with the surrounding environment through aerial return paths, the analytical representation of realistic channels is non-trivial. Semi-analytical numerical electromagnetic methods are quite useful for investigating these phenomena and gaining a deep insight into the underlying physics, such as ray tracing, the method of moment (MoM), the finite-difference time-domain (FDTD), and the finite element method (FEM). In particular, the FEM is especially suitable for analyzing structures with curved boundaries (e.g., the human body), as its analysis depends on dividing large structures into smaller isoparametric shapes of various geometries, e.g., triangular and rectangular. Therefore, the FEM has extensively been used to simulate both galvanic and capacitive body channels.

For simulations, we used ANSYS's high-frequency structure simulator (HFSS), a 3D electromagnetic simulation software for designing and simulating high-frequency electronic products[‡]. In order to reduce simulation time complexity, we employed HFSS's high-performance computing (HPC) feature to accelerate its built-in sophisticated solvers. Indeed, its automatic adaptive meshing techniques are especially suitable for a computer-aided-design (CAD)-based numerical body phantom. Thus, we exploit the NEVA's anatomical true-CAD human model [17], which is created based on the high-resolution cryosection image dataset from the Visible Human Project (VHP) Female of the U.S. National Library of Medicine [18]. NEVA is a voxel-based full-body numerical human body phantom that segments the human body into 26 different tissue types (e.g., muscle, fat, bone, skin, etc.) and 184 individual tissue parts, each of which is assigned to corresponding permittivity and conductivity parameters. We must note that NEVA is available to all interested research practitioners free of charge through the application form on the NEVA website[§].

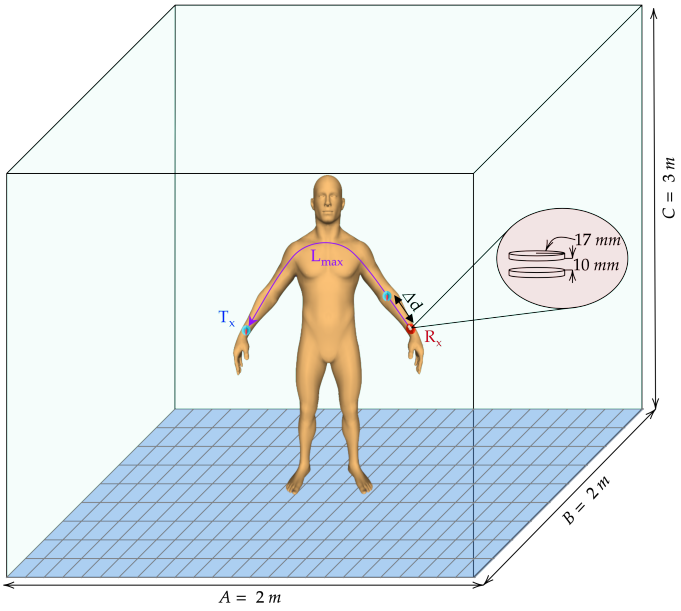

Fig. 3: Simulation setup using the NEVA model in HFSS.

TABLE I: Polynomial coefficients for channel and frequency dependent parametric path loss model.

$\mathbf{PL}(\ell,\mathbf{f}) = \sum_{\mathbf{m}=0}^{\mathbf{1}} \sum_{\mathbf{n}=0}^{\mathbf{4}} \mathbf{c_{m,n}} \ell^{\mathbf{m}} \mathbf{f}^{\mathbf{n}}$, $\mathbf{PL}$ [dB], ℓ [cm], $\mathbf{f}$ [MHz]						
$\mathbf{c_{m,n}}$		m				
		0	1	2	3	4
n	0	43.21	0.06583	-0.02426	3.582E-4	-1.308E-6
	1	0.1501	1.074E-3	-1.104E-5	4.615E-8	0
Goodness of Fit						
$\mathbf{R^2}$		SSE		RMSE		
1		0.0588		0.01147		

Throughout the paper, we consider the simulation set up demonstrated in Fig. 3, where the NEVA model is placed in the center of a room A x B x C meters in size. Similar to commercial off-the-shelf electrodes, transceiver's signal and ground electrodes are designed as circular metallic plates with a 17 mm radius and a 10 mm vertical separation. While the receiver is fixed to the left wrist, the transmitter is iteratively relocated towards the right wrist with Δ_d displacement steps until it reaches the right wrist. Since the maximum channel length between the wrists $\mathrm{L_{max}}$ is 120 cm, setting $\Delta_d = 5$ cm yields overall 25 measurement locations. On the other hand, we consider $\Delta_f = 5$ MHz frequency increments between 10-100 MHz. Based on Tx/Rx locations mentioned above, the path loss between the receiver and transmitter placed at i^{th}, $2 \leqslant i \leqslant 25$ is calculated based on the S-parameters at the frequency of interest. The individual curve fittings of the

[‡]Please see company website for more information https://www.ansys.com/products/electronics/ansys-hfss.

[§]https://www.nevaelectromagnetics.com/vhp-female-2-2

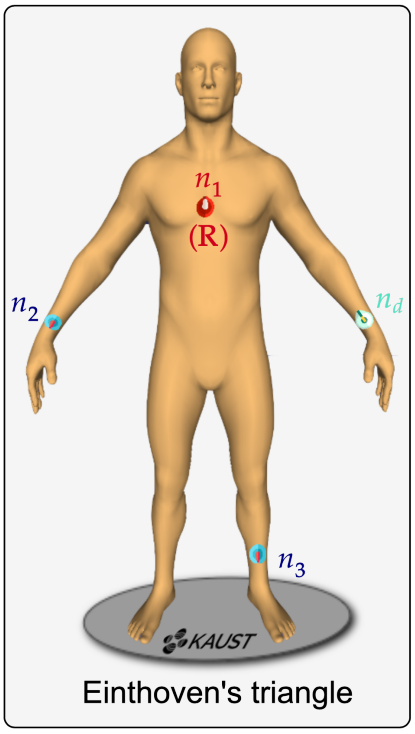

(a) Einthoven's Triangle

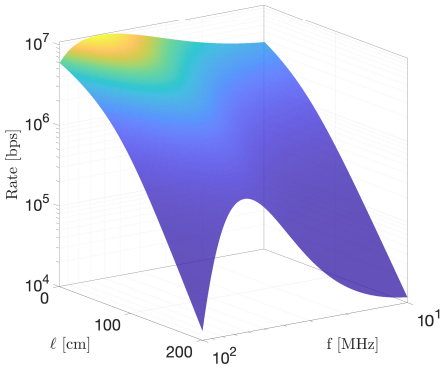

(b) A single node's rate w.r.t. channel frequency and length ($P = -60$ dBm).

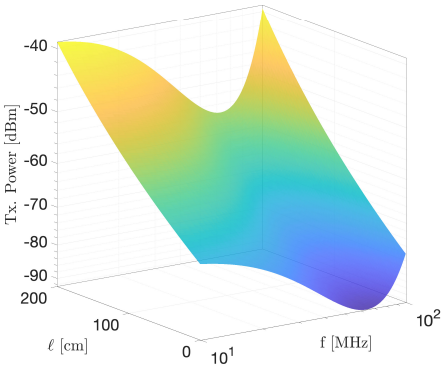

(c) A single node's transmit power w.r.t. channel frequency and length (R=1 Mbps).

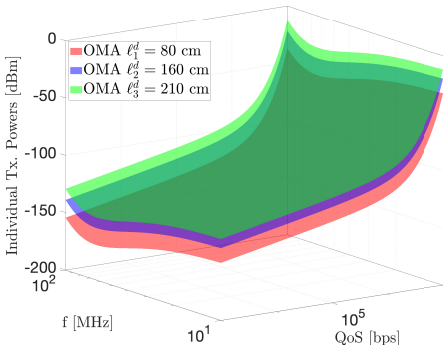

(d) OBA individual transmit powers w.r.t. frequency and rate.

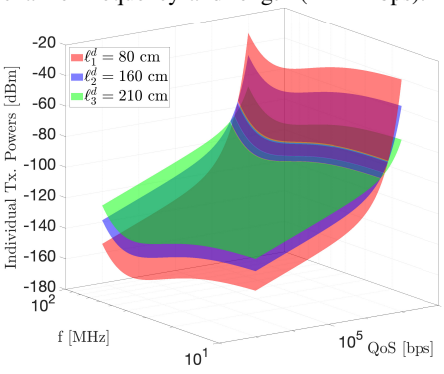

(e) NOBA individual transmit powers w.r.t. frequency and rate.

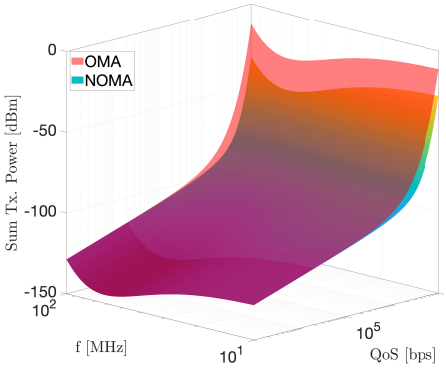

(f) OBA and NOBA total transmit power w.r.t. frequency and rate.

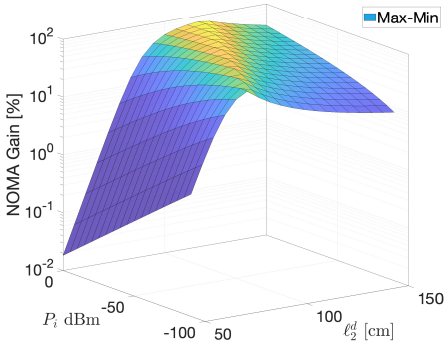

(g) NOBA max-min rate gain w.r.t. transmission power and channel length.

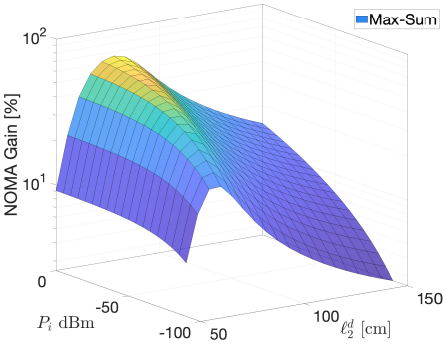

(h) NOBA max-sum rate gain w.r.t. transmission power and channel length.

Fig. 4: Comparison of OBA and NOBA schemes for different performance metrics under various system parameters.

path loss for various channel length and frequency initially suggested that a linear and the fourth-order polynomial fits are sufficient to characterize the path loss variations with respect to channel length and frequency, respectively.

By using HFFS simulation results in Matlab's curve fitting tool, we obtain the following path loss fitting model

$$\mathrm{PL}(\ell, \mathrm{f}) = \sum_{\mathrm{m}=0}^{1} \sum_{\mathrm{n}=0}^{4} \mathrm{c}_{\mathrm{m,n}} \ell^{\mathrm{m}} \mathrm{f}^{\mathrm{n}}, \mathrm{PL[dB]}, \ell\mathrm{[cm]}, \mathrm{f[MHz]}, \quad (47)$$

where $\mathrm{c}_{\mathrm{m,n}}$ are the polynomial coefficients, ℓ is channel length, and f is the channel frequency. Table I lists the coefficients and goodness of fit metrics such as R-square, degree-of-freedom (DoF)-adjusted R-square, the sum of squares due to error (SSE), and the root mean squared error (RMSE). Having both R-square and DoF-adjusted-R-square value equal to one indicates that the model explains the data variation relatively well with low error components, since both SSE and RMSE also attain relatively low values. Accordingly, the path loss between n_i and n_j, $\mathrm{PL}_{\mathrm{i}}^{\mathrm{j}}$, can be computed by substituting ℓ_i^j and the operational frequency f into (47). Lastly, the linear scale channel gain between n_i and n_j is obtained by $h_i^j = 10^{-\mathrm{PL}_{\mathrm{i}}^{\mathrm{j}}/10}$.

B. Impacts of Channel Length and Operating Frequency

Let us first consider a single node to investigate channel length and frequency dependent behavior of data rate and transmission power. Fig. 4b shows the achievable data rate with respect to channel length and frequency for a node with

-60 dBm transmit power. While the data rate monotonically decreases with increasing channel length, it reaches a peak around 65 MHz and starts decreasing afterwards. A reciprocal relation is observed in Fig. 4c where required transmission power to reach 1 Mbps data rate is shown with respect to various channel length and frequency. Observing the maximum rate and minimum transmission power around 65 MHz is directly related to the frequency dependent path loss of capacitive body channels [19]. Although 65 MHz provides superior throughput and energy efficiency, it is more vulnerable to overhearing and eavesdropping due to higher signal leakage. It is shown in [7] that operating at 10 MHz limits the signal leakage to 15 cm around the body and provides a better physical layer security at the expense of relatively more power consumption. Indeed, this tradeoff can pave the way for dynamic channel access schemes where nodes can switch to different operational frequency levels to strike a balance between physical layer security and throughput efficiency. At this point, it is necessary to compare the BCC with 10 mW/Mbps transmit power efficiency of the BLE. It is obvious from Fig. 4c that BCC can reach 1 Mbps with up to 50-100 dBm less transmission power. We should note that this performance enhancement comparison is subject to path loss characteristics of both BCC and 2.4 GHz ISM band. The capacitive body channel path loss is affected by grounding effects, variable impedance of electrode-skin interface, and impedance matching imperfections. On the other hand, the ISM bands are subject to heavy shadow fading caused by the lossy dielectric nature of the human body, which alters the antenna features by detuning impedance matching, modifying radiation pattern, shifting the resonant frequency, and eventually reducing the overall efficiency [1].

To investigate the transmit power as function of the QoS demands, let us now consider an IoB network in Fig. 4a where node locations are inspired from Einthoven's triangle. For a human subject of 185 cm height, the channel lengths are given by $\ell_1^d = 85$ cm, $\ell_2^d = 150$ cm, and $\ell_3^d = 210$ cm. In Fig. 4d and Fig. 4e, we depict the individual power consumption of each node for the OBA and NOBA schemes, respectively. Fig. 4e shows that transmit power level order, and hence the decoding order, changes as QoS demand increases. On the contrary, transmit power level of the OBA scheme is inversely proportional to the path loss and does not change as each node operate on a dedicated bandwidth portion with its own power source. Fig. 4f shows the total transmission power with respect to QoS demand and frequency under QoS sufficient regime as it is especially suitable to maximize the network lifetime given the QoS demands are met. It is obvious that non-orthogonal body channel access become significantly power efficient as the QoS demand increases. This is mainly because of optimizing the powers for the throughput efficient nature of non-orthogonal access.

Defining the gain by the ratio of NOBA rate to that of OBA, Fig. 4g and Fig. 4h show the max-min and max-sum rate gains with respect to different transmission powers and channel lengths ℓ_2^d ($\ell_1^d = 50$ cm), respectively. Even though NOBA delivers a better max-min rate than OBA, its gain is determined by the transmission powers and the relative channel length of the far-away node to the closer node. Fig. 4g shows that NOBA is especially beneficial to deliver higher max-min fairness as the second node gets away from the destination node. On the other hand, the NOBA max-sum rate gain monotonically increases with the transmission power while it reaches a peak around $\ell_2^d = 70$ cm and starts decreasing afterward. This is mainly because of the fact that the compensating the worsening low channel gain of the second node destroys the contribution of the first node to the overall sum rate.

C. Max-Min Rate Regime

This section compares access schemes under the max-min regime with different node deployment scenarios, maximum transmission powers, and the number of nodes. In Fig. 5a, we consider n_1 and n_2, where we select n_1 as the relay node in the cooperative cases. We set channel length from the first node to the destination to $\ell_1^d = 50$ cm and increase the channel length from the second node to the first node ℓ_2^1 up to 200 cm, which is sufficiently long for a human subject of height 185 cm. Fig. 5a compares max-min rate performance of regular and cooperative orthogonal and non-orthogonal access schemes with $P_i = -60$ dBm and $P_i = -90$ dBm maximum transmission powers. At $P_i = -60$ dBm, non-orthogonal access schemes deliver better performance than their orthogonal counterparts in both regular and cooperative cases. However, it is interesting to see that cooperation starts helping when the second node is around 100 cm and 125 cm far away from the relay node in orthogonal and non-orthogonal schemes, respectively. At $P_i = -90$ dBm, however, cooperation becomes beneficial immediately and significantly after $\ell_2^1 = 20cm$ while the regular non-orthogonal scheme is almost the same as the regular orthogonal scheme. Indeed, these behaviors are directly related to the received power levels. Since the received power levels are significantly lower than $P_i = -60$ dBm case, the cooperation becomes more effective even at very short channel lengths between the relay and the second node. Likewise, as the transmission power decreases, received power levels and thus the caused interference reduces. As a direct result, the interference cancellation does not contribute to having a significant non-orthogonal access gain.

In Fig. 5b, we fix the channel length between the source and destination nodes to $\ell_2^d = 150$ cm while placing the relay node to $\ell_1^d = 50$ cm and $\ell_1^d = 100$ cm away from the destination node. Fig. 5b compares max-min rate performance of regular and cooperative orthogonal and non-orthogonal access schemes at maximum transmission powers ranging from -90 dBm to 0 dBm. It is obvious from Fig. 5b that cooperation improves the performance significantly as the channel length ratio between the source and relay (i.e., ℓ_2^d/ℓ_1^d) increases and maximum transmission power decreases. One can observe that regular orthogonal and non-orthogonal scheme performs better than others at $\ell_1^d = 50$ cm and above -60 dBm. It is also interesting to see that the regular non-orthogonal scheme at $\ell_1^d = 100$ cm reaches the regular non-orthogonal scheme at $\ell_1^d = 50$ around -30 dBm transmission power and above.

In Fig. 5c, we fix the channel length between the relay and destination nodes to $\ell_1^d = 50$ cm and place the ith source

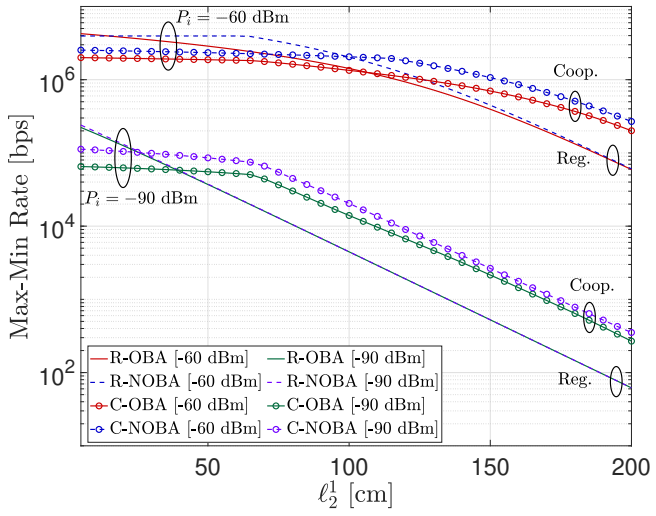

(a) Max-Min rate vs. ℓ_2^1 [$\ell_1^d = 50$ cm].

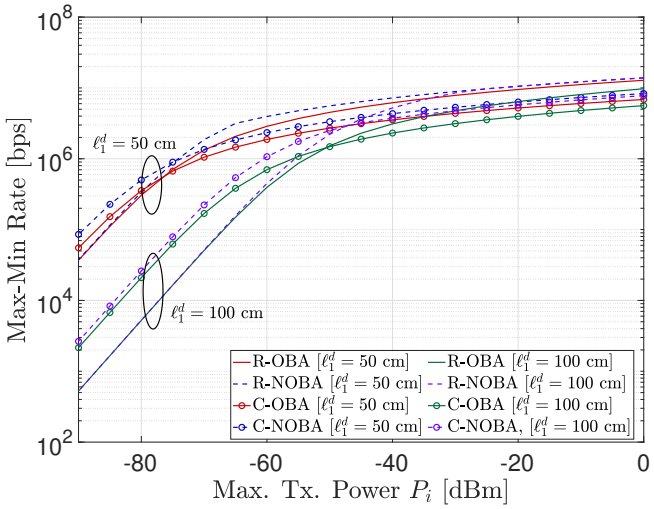

(b) Max-Min rate vs. P_i [$\ell_2^d = 150$ cm].

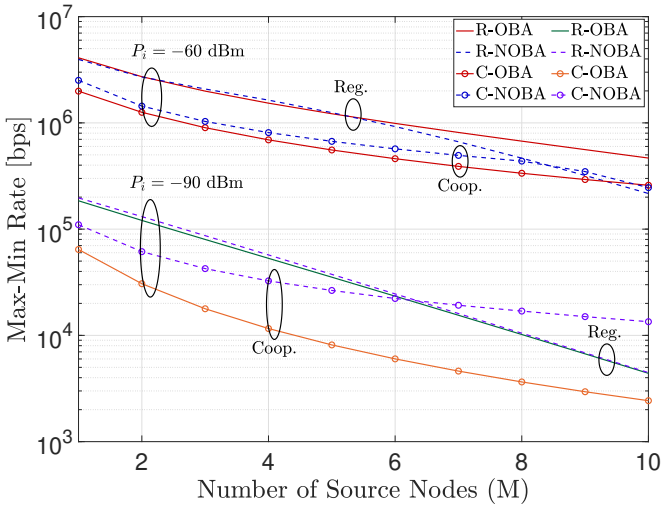

(c) Max-Min rate vs. number of source nodes.

Fig. 5: Comparison of capacitive body channel access schemes under the max-min rate regime.

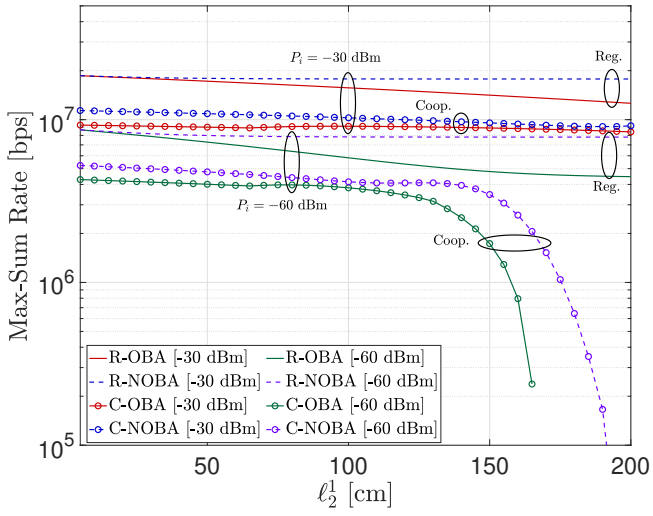

(a) Max-Sum rate vs. ℓ_2^1 [$\ell_1^d = 50$ cm].

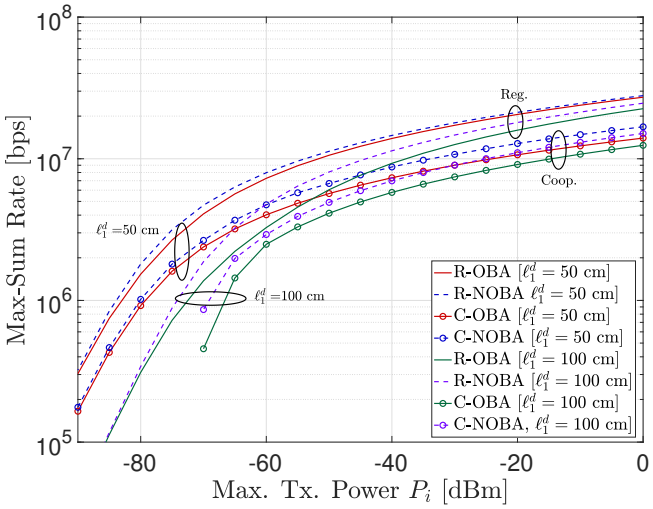

(b) Max-Sum rate vs. P_i [$\ell_2^d = 150$ cm].

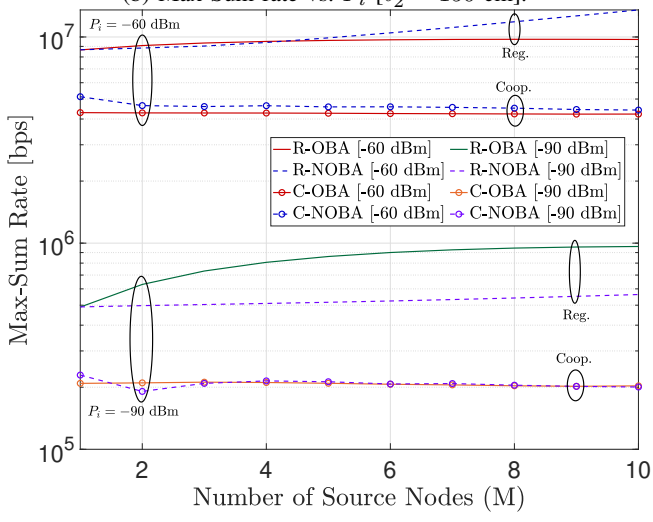

(c) Max-Sum rate vs. number of source nodes.

Fig. 6: Comparison of capacitive body channel access schemes under the max-sum rate regime.

node $i \times 5$ cm away from the relay node, $1 \leqslant i \leqslant M$. It is obvious from Fig. 5c that adding more nodes to the IoB network decreases the max-min rate. At $P_i = -60$ dBm, the regular and cooperative non-orthogonal schemes start performing worse than their orthogonal counter parts after $M = 5$ and $M = 10$, respectively. This is mainly because of adding more nodes cause more interference and thus performance degradation. At $P_i = -60$ dBm, however, regular orthogonal and non-orthogonal schemes deliver similar max-min rates as the accumulated interference is not significant due to the low transmission powers. Both at $P_i = -60$ dBm and $P_i = -90$ dBm, the cooperation cause significant performance degradation for orthogonal schemes. On the other hand, it become beneficial for non-orthogonal schemes after $M = 9$ and $M = 6$ for $P_i = -60$ dBm and $P_i = -90$ dBm maximum transmission powers.

D. Max-Sum Rate Regime

This section compares access schemes under the max-sum regime with different node deployment scenarios, maximum transmission powers, and the number of nodes. Similar to Fig. 5a, Fig. 6a also considers n_1 and n_2, where n_1 is selected as the relay node in the cooperative cases. We set channel length from the first node to the destination to $\ell_1^d = 50$ cm and increase the channel length from the second node to the first node ℓ_2^1 up to 200 cm. Fig. 6a compares max-sum rate performance of regular and cooperative orthogonal and non-orthogonal access schemes with $P_i = -30$ dBm and $P_i = -60$ dBm maximum transmission powers. The regular orthogonal scheme experiences performance degradation at both maximum transmission powers as the source nodes get away from the source and destination nodes. On the contrary, the regular non-orthogonal scheme is able to sustain a stable sum-rate. This is a direct result of the power allocation that allows the source node to transmit at high powers to compensate for the bad channel conditions. The same behavior can also be observed between cooperative orthogonal and non-orthogonal schemes. The most noteworthy observation in Fig. 6a is that the cooperation does not provide any performance enhancement over the regular case because the maximum transmission power of the relay node is shared for both nodes. This naturally constitutes a bottleneck, and optimizing the phase-time allocation cannot mitigate this destructive effect. Notice that this is not the case for the max-min rate regime, where the cooperation is useful as the source nodes moves away from the destination node. Please also notice for $P_i = -60$ dBm that the network degrades significantly for $\ell_2 > 150$ cm as it becomes infeasible to satisfy QoS requirements.

Similar to Fig. 5b, Fig. 5b also fixes the channel length between the source and destination nodes to $\ell_2^d = 150$ cm while placing the relay node to $\ell_1^d = 50$ cm and $\ell_1^d = 100$ cm away from the destination node. Fig. 6b compares max-sum rate performance of regular and cooperative orthogonal and non-orthogonal access schemes at maximum transmission powers ranging from -90 dBm to 0 dBm. It is obvious from Fig. 6b that the network sum-rate improves as the maximum transmission power increases. However, the cooperation still delivers a poor performance because of the same reasons mentioned above. It is also interesting to see that the regular schemes at $\ell_1^d = 100$ cm perform better than cooperative cases at $\ell_1^d = 50$ starting from -55 dBm and - 65 dBm for orthogonal and non-orthogonal schemes, respectively.

In Fig. 6c, we fix the channel length between the relay and destination nodes to $\ell_1^d = 50$ cm and place the ith source node $i \times 5$ cm away from the relay node, $1 \leqslant i \leqslant M$. Contrary to the max-min rate trend shown in Fig. 5c, adding more nodes to the IoB network improves the max-sum rate at regular access schemes more significant for non-orthogonal schemes due to their innate spectral efficiency. Similar to Fig. 6a and Fig. 6b, cooperative schemes deliver a poorer performance than their regular counterparts at all times.

VI. Conclusion

Thanks to the parallel advancements in signal processing, wireless communications, and digital circuits, the IoB is expected to be an integral part of our daily lives Especially, non-invasive on-body IoB nodes can play a vital role to transform e-health by enabling preventive health-care through constant and comfortable monitoring of patients. However, achieving this goal by means of conventional RF systems due to their power-hungry, bulky, interference limited, and physically unsecure nature. Therefore, this paper considered BCC as an alternative form of communications and evaluated the performance of an IoB network that operates on orthogonal and non-orthogonal access schemes with and without cooperation. Optimization of power and phase-time allocations are studied for various QoS regimes. In order to provide a deep insight into how cooperation can improve the end-to-end performance, extensive numerical results are presented to compare these schemes under key design parameters.

References

[1] A. Celik, K. N. Salama, and A. Eltawil, "The internet of bodies: A systematic survey on propagation characterization and channel modeling," Sep 2020. [Online]. Available: http://hdl.handle.net/10754/664925

[2] S. Movassaghi, M. Abolhasan, J. Lipman, D. Smith, and A. Jamalipour, "Wireless body area networks: A survey," *IEEE Commun. Surveys Tuts.*, vol. 16, no. 3, pp. 1658–1686, Third 2014.

[3] "Ieee standard for wireless body area networks," *IEEE Std 802.15.6-2012*, pp. 1–271, Feb. 2012.

[4] J. Mao, H. Yang, and B. Zhao, "An investigation on ground electrodes of capacitive coupling human body communication," *IEEE Trans. Biomed. Circuits Syst.*, vol. 11, no. 4, pp. 910–919, 2017.

[5] P. S. Hall *et al.*, "Antennas and propagation for on-body communication systems," *IEEE Antennas Propag. Mag.*, vol. 49, no. 3, pp. 41–58, 2007.

[6] H. Baldus, S. Corroy, A. Fazzi, K. Klabunde, and T. Schenk, "Human-centric connectivity enabled by body-coupled communications," *IEEE Commun. Mag.*, vol. 47, no. 6, pp. 172–178, 2009.

[7] D. Das, S. Maity, B. Chatterjee, and S. Sen, "Enabling covert body area network using electro-quasistatic human body communication," *Sci. Reports*, vol. 9, no. 1, pp. 1–14, 2019.

[8] H. Cho, H. Kim, M. Kim, J. Jang, Y. Lee, K. J. Lee, J. Bae, and H. Yoo, "A 79 pj/b 80 mb/s full-duplex transceiver and a 42.5μW 100 kb/s super-regenerative transceiver for body channel communication," *IEEE Journal of Solid-State Circuits*, vol. 51, no. 1, pp. 310–317, 2016.

[9] S. Maity, B. Chatterjee, G. Chang, and S. Sen, "Bodywire: A 6.3-pj/b 30-mb/s -30-db sir-tolerant broadband interference-robust human body communication transceiver using time domain interference rejection," *IEEE Journal of Solid-State Circuits*, vol. 54, no. 10, pp. 2892–2906, 2019.

[10] J.-H. Lee, K. Kim, M. Choi, J.-Y. Sim, H.-J. Park, and B. Kim, "A 16.6-pj/b 150-mb/s body channel communication transceiver with decision feedback equalization improving> 200% area efficiency," in *2017 Symposium on VLSI Circuits*. IEEE, 2017, pp. C62–C63.
[11] A. Celik, R. M. Radaydeh, F. S. Al-Qahtani, A. H. A. El-Malek, and M.-S. Alouini, "Resource allocation and cluster formation for imperfect noma in dl/ul decoupled hetnets," in *Proc. IEEE Globecom Workshops (GC Wkshps)*, 2017, pp. 1–6.
[12] A. Celik, M. Tsai, R. M. Radaydeh, F. S. Al-Qahtani, and M. Alouini, "Distributed user clustering and resource allocation for imperfect noma in heterogeneous networks," *IEEE Transactions on Communications*, vol. 67, no. 10, pp. 7211–7227, 2019.
[13] S. Arzykulov, A. Celik, G. Nauryzbayev, and A. M. Eltawil, "Uav-assisted cooperative & cognitive NOMA: deployment, clustering, and resource allocation," *CoRR*, vol. abs/2008.11356, 2020. [Online]. Available: https://arxiv.org/abs/2008.11356
[14] A. Celik, M. Tsai, R. M. Radaydeh, F. S. Al-Qahtani, and M. Alouini, "Distributed cluster formation and power-bandwidth allocation for imperfect noma in dl-hetnets," *IEEE Transactions on Communications*, vol. 67, no. 2, pp. 1677–1692, 2019.
[15] R. D. Yates, "A framework for uplink power control in cellular radio systems," *IEEE Journal on Selected Areas in Communications*, vol. 13, no. 7, pp. 1341–1347, 1995.
[16] M. Grant and S. Boyd, "CVX: Matlab software for disciplined convex programming, version 2.1," http://cvxr.com/cvx, Mar. 2014.
[17] S. N. Makarov, G. M. Noetscher, J. Yanamadala, M. W. Piazza, S. Louie, A. Prokop, A. Nazarian, and A. Nummenmaa, "Virtual human models for electromagnetic studies and their applications," *IEEE Reviews in Biomedical Engineering*, vol. 10, pp. 95–121, 2017.
[18] C. Waldby, *The visible human project: Informatic bodies and posthuman medicine*. Psychology Press, 2000.
[19] Q. T. Nguyen, A. Celik, K. N. Salama, and A. Eltawil, "Statistical and parametric channel modeling for capacitive body channel communications," Mar. 2021.

Abdulkadir Celik (Senior Member, IEEE) received the M.S. degree in electrical engineering in 2013, the M.S. degree in computer engineering in 2015, and the Ph.D. degree in co-majors of electrical engineering and computer engineering in 2016 from Iowa State University, Ames, IA, USA. He was a post-doctoral fellow at King Abdullah University of Science and Technology (KAUST) from 2016 to 2020. Since 2020, he has been a research scientist at the communications and computing systems lab at KAUST. His research interests are in the areas of wireless communication systems and networks.

Ahmed M. Eltawil (Senior Member, IEEE) received the M.Sc. and B.Sc. degrees (Hons.) from Cairo University, Giza, Egypt, in 1999 and 1997, respectively, and the Ph.D. degree from the University of California, Los Angeles, CA, USA, in 2003. Since 2019, he has been a Professor with the Computer, Electrical and Mathematical Science and Engineering Division (CEMSE), King Abdullah University of Science and Technology (KAUST), Thuwal, Saudi Arabia. Since 2005, he has been with the Department of Electrical Engineering and Computer Science, University of California at Irvine, where he founded the Wireless Systems and Circuits Laboratory. His research interests are in the general area of low power digital circuit and signal processing architectures with an emphasis on mobile systems. He has been on the technical program committees and steering committees for numerous workshops, symposia, and conferences in the areas of low power computing and wireless communication system design. He received several awards, as well as distinguished grants, including the NSF CAREER Grant supporting his research in low power systems.